Bio-Design and Manufacturing (2025) 8:1024–1034
https://doi.org/10.1631/bdm.2500047

RESEARCH ARTICLE

Bio-inspired magnetic soft robot with dual-modal locomotion for enhanced liquid–air interface navigation

Chonglei Hao[1] · Binhong Dou[1] · Shenghao Yang[1] · Haochen Wang[2] · Lei Zhang[1] · Bing Li[1] · Qing Cao[3,4] · Huayong Yang[3,4] · Dong Han[3,4] · Fuzhou Niu[2,3]

Received: 5 February 2025 / Accepted: 18 March 2025

Abstract

Small-scale magnetic soft robots are promising candidates for minimally invasive medical applications; however, they struggle to achieve efficient locomotion across various interfaces. In this study, we propose a magnetic soft robot that integrates two distinct bio-inspired locomotion modes for enhanced interface navigation. Inspired by water striders' superhydrophobic legs and the meniscus climbing behavior of *Pyrrhalta nymphaeae* larvae, we developed a rectangular sheet-based robot with hydrophobic surface treatment and novel control strategies. The proposed robot implements two locomotion modes: a bipedal peristaltic locomotion mode (BPLM) and a single-region contact-vibration locomotion mode (SCLM). The BPLM achieves stable movement at 20 mm/s through coordinated front–rear contact points, whereas the SCLM reaches an ultrafast speed of 52 mm/s by optimizing surface tension interactions. The proposed robot demonstrates precise trajectory control with minimal deviations and successfully navigates confined spaces while manipulating objects. Theoretical analysis and experimental validation demonstrate that the integration of triangular wave control signals and steady-state components enables smooth transitions between locomotion modes. This study presents a new paradigm for bio-inspired design of small-scale robots and demonstrates the potential for medical applications requiring precise navigation across multiple terrains.

Chonglei Hao, Binhong Dou, and Shenghao Yang have contributed equally to this work.

✉ Dong Han
dong_han@zju.edu.cn

✉ Fuzhou Niu
fzniu@usts.edu.cn

[1] School of Robotics and Advanced Manufacture, Harbin Institute of Technology, Shenzhen 518055, China

[2] School of Mechanical Engineering, Suzhou University of Science and Technology, Suzhou 215009, China

[3] State Key Laboratory of Fluid Power and Mechatronic Systems, Zhejiang University, Hangzhou 310058, China

[4] School of Mechanical Engineering, Zhejiang University, Hangzhou 310058, China

Graphical abstract

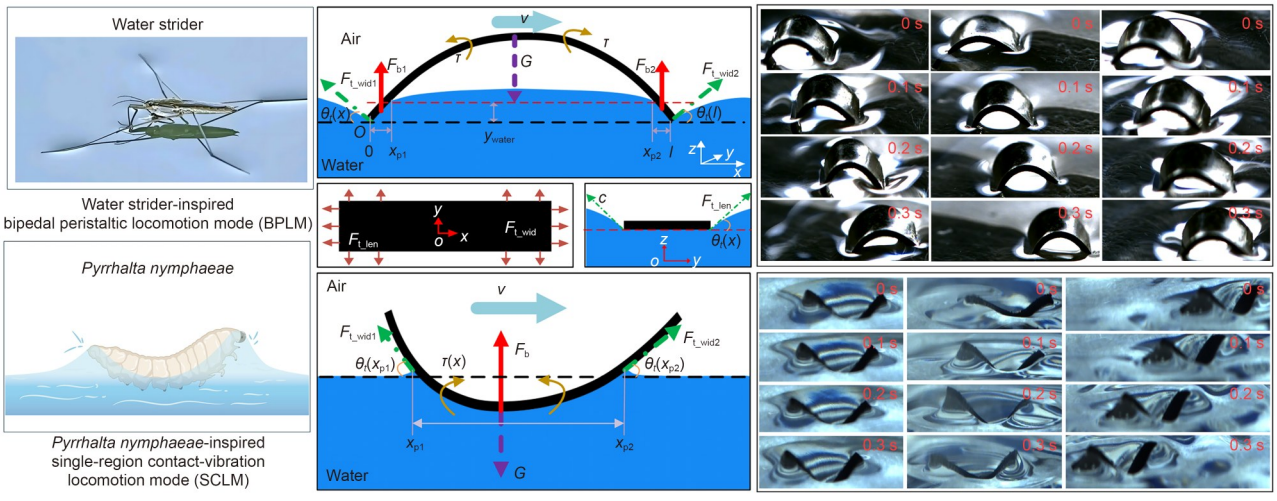

Keywords Magnetic soft robot · Dual bio-inspired locomotion · Interface navigation · Water strider · *Pyrrhalta nymphaeae* larvae

1 Introduction

Small-scale magnetic actuated robots have garnered significant attention in biomedical applications because of their potential for minimally invasive procedures, targeted drug delivery, and cell manipulation [1–6]. These robots have unique advantages, including wireless operation, precise control, and biocompatibility [7–9]. However, when navigating complex biological environments, particularly across various interfaces, these robots face significant challenges in maintaining efficient locomotion and adaptability [10–13].

Recent advances in magnetic soft robots have led to the development of various locomotion strategies [5, 14–16]. Ren et al. developed soft robots capable of crawling and swimming through different media, achieving speeds of up to 15 mm/s [17]. Gu et al. reported magnetically actuated artificial cilia that generate synchronized waves for surface movement even though they are limited to specific interfaces [18]. Wang et al. achieved controlled swimming capabilities through magnetic actuation but faced challenges in maintaining stability across interfaces [19]. Although Lu et al. demonstrated multilegged locomotion under both dry and wet conditions, their design exhibited reduced efficiency in confined spaces [20]. Niu et al. developed a heat-assisted in-situ magnetic domain programming method that enables the fabrication of magnetically soft robots with complex three-dimensional (3D) domain distributions, offering a bio-inspired approach to achieve multi-modal locomotion reminiscent of natural organisms [21]. Nature provides inspiring examples of organisms that excel at interface navigation [22–25]. Water striders can effortlessly walk on liquid surfaces because of their superhydrophobic legs and specialized motion patterns, achieving remarkable speed and stability [26, 27]. Similarly, *Pyrrhalta nymphaeae* larvae exhibit exceptional meniscus climbing abilities through sophisticated surface tension manipulation [28, 29]. Although these biological systems have inspired various robotic designs, the integration of multiple bio-inspired locomotion strategies within a single platform remains largely unexplored, particularly for small-scale magnetic robots.

In this study, a magnetic soft robot with dual bio-inspired locomotion modes was developed. The robot design is inspired by two distinct biological systems: the superhydrophobic legs of water striders and the meniscus climbing behavior of *Pyrrhalta nymphaeae* larvae. Based on these biological principles, two complementary locomotion modes, namely, the bipedal peristaltic locomotion mode (BPLM) and the single-region contact-vibration locomotion mode (SCLM), were successfully implemented. Detailed modeling of the developed robot was performed to ensure that its motion was controllable. In addition, a triangular wave control signal with steady-state components was developed, through which smooth transitions between the two locomotion modes were achieved. Precise trajectory control was demonstrated with minimal deviations in both the x- and y-direction. Mathematical models were established to analyze the surface tension effects and magnetic actuation mechanisms, through which the relationship between the control signals and robot behavior was thoroughly investigated. These achievements were validated through multiple rounds of testing, systematic parameter optimization, and detailed comparative studies. The developed robot demonstrates

significant advantages over existing systems in terms of movement speed, trajectory control, and adaptability to different interfaces. These capabilities, combined with the small scale and magnetic actuation of the robot, make it particularly suitable for medical applications requiring careful navigation through biological interfaces.

2 Bio-inspired locomotion

2.1 Structure design, magnetization, and dynamic modeling

Small-scale robots capable of navigating liquid–air interfaces represent a significant advancement in biomimetic engineering. This study proposes a magnetic soft robot design that draws inspiration from natural organisms, implementing their sophisticated surface interaction strategies through engineered solutions.

The proposed robot adopts a rectangular sheet configuration, as shown in Fig. 1a, where l represents the length and w represents the width. The thickness h critically determines both bending strength and magnetization intensity, enabling strong magnetic torque generation at given field strengths. The fabrication process employs NdFeB particles (38-μm diameter) and silica gel (Ecoflex-00-30, Smooth-On, Inc., USA) mixed at a 1:1 mass ratio. Following vacuum degassing and thermal curing at 65 °C for 8 h, the resulting membrane undergoes magnetization in a circular mold (Fig. 1b). The details of the robot fabrication are presented in Note S1 in the supplementary information. The magnetization angle θ_0 (shown in Fig. 1b) of the robots we manufactured and used in the experiments is π, and in the subsequent dynamic modeling, θ_0 still represents the magnetization angle to maintain the generality of the model.

The magnetization process follows a specialized method in which $\beta(x)$ denotes the direction of magnetization inside the robot (Fig. 1c). Magnetization is achieved using a circular mold, ensuring uniform alignment of the internal magnetic field. After the flattening process, the internal magnetization direction based on the coordinate system of the robot can be expressed as follows:

$$\beta(x) = -\frac{x}{r} - \theta_0 + \frac{\pi}{2},$$

where r represents the radius of curled magnetization, which determines the deformation state of the robot.

The theoretical framework models the bending behavior under external forces by incorporating the torque, field

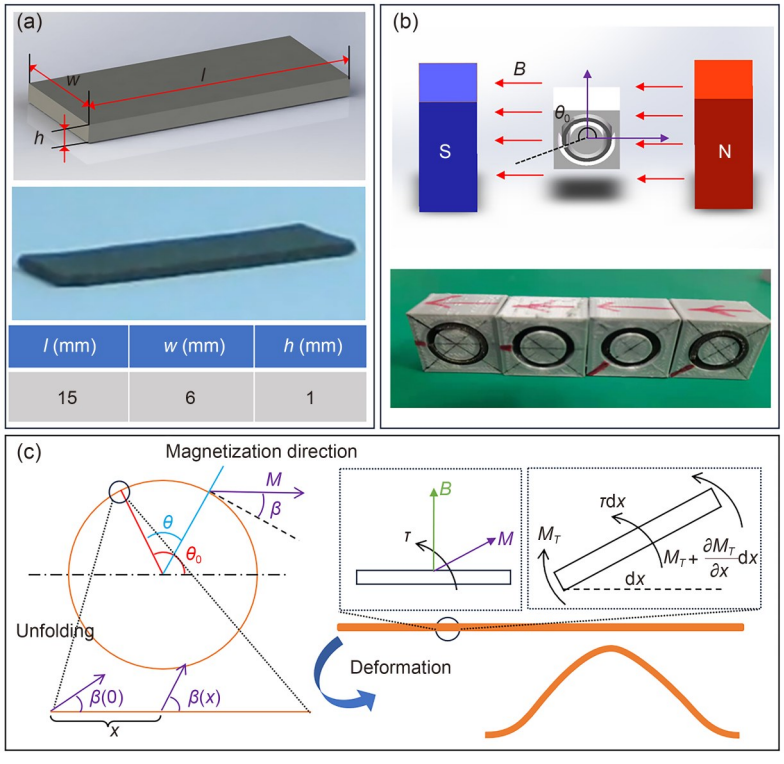

Fig. 1 Structural design, fabrication, initial magnetization modeling, and theoretical deformation modeling of the magnetic soft robot. (a) Configuration with key dimensions and a fabricated sample. (b) Magnetization process using a circular mold to achieve tailored internal magnetization. Here, θ_0 denotes the angle between the robot's gap and the direction of the magnetic field. (c) Schematic diagrams of the magnetization model and force-induced deformation model of the robot. $\beta(x)$ represents the direction of the magnetization intensity at point x after the robot unfolds. The figure on the right shows the mechanical model of the robot deformation under the z-axis magnetic field

strength, and material elasticity (Fig. 1c). Force analysis illustrates how the robot achieves stable locomotion through optimized torque distribution and deformation under an applied magnetic field. Under an external magnetic field, the deformation of the robot on the *xoz* plane follows the Euler–Bernoulli beam model (as shown in Fig. 1c):

$$y(x) = \frac{r^3 AM}{EI}\left[-\cos\theta_z \sin\left(\frac{x}{r} + \theta_0\right),\right.$$
$$\left.\sin\theta_z \sin\left(\frac{x}{r} + \theta_0\right), \quad \cos\left(\frac{x}{r} + \theta_0\right)\right]\begin{bmatrix} B_x \\ B_y \\ B_z \end{bmatrix},$$

where A is the cross-sectional area of the robot, M represents the magnetization intensity, E represents Young's modulus, I represents the cross-sectional moment of inertia, $[B_x \quad B_y \quad B_z]^{\mathrm{T}}$ represents the magnetic flux density in the fixed base coordinate system, and θ_z denotes the angle between the z axes of the robot's coordinate system and the fixed base coordinate system.

The rotational angles around the z-axis are governed by

$$\phi(t) = \frac{-rAM\left(B_x \sin\theta_z + B_y \cos\theta_z\right)\cos\left(\frac{x}{r} + \theta_0\right) + M_{\mathrm{d}}}{J_z} t^2,$$

where J_z denotes the rotational moment of inertia, t represents the duration of magnetic field activation, and M_{d} denotes the drag moment.

During locomotion at liquid–air interfaces, the robot is controlled via multiple force elements, including gravity G, buoyancy F_{b}, surface tension $\boldsymbol{F}_{\mathrm{t}}$, and hydrodynamic drag F_{drag}. These forces collectively influence the motion characteristics and stability of the robot on water surfaces.

Motion control and deformations are achieved through a 3D Helmholtz coil system that generates magnetic fields dynamically as follows:

$$\begin{bmatrix} B_x \\ B_y \\ B_z \end{bmatrix} = \begin{bmatrix} \sqrt{B_{\mathrm{Xcoil}}^2 + B_{\mathrm{Zcoil}}^2}\cos\varphi\cos\theta_{\mathrm{r}} \\ \sqrt{B_{\mathrm{Xcoil}}^2 + B_{\mathrm{Zcoil}}^2}\cos\varphi\sin\theta_{\mathrm{r}} \\ \sqrt{B_{\mathrm{Xcoil}}^2 + B_{\mathrm{Zcoil}}^2}\sin\varphi \end{bmatrix},$$

where B_{Xcoil} and B_{Zcoil} denote the magnetic field strengths of the x and z coils, respectively, $\varphi = \arctan\left(B_{\mathrm{Zcoil}}/B_{\mathrm{Xcoil}}\right)$ denotes the angle between the magnetic field and the *xoz* plane, and θ_{r} denotes the rotation angle of the rotating base. This configuration enables precise control over the robot's movement.

Deformation under external forces is further influenced by the material properties of the beam. Inspired by natural systems, the fabricated robots were further treated with a commercial coating agent to render their surface superhydrophobic, with the exhibited water droplet contact angle up to approximately 152°. This bio-inspired approach demonstrates how natural principles can be effectively translated into engineered systems, opening new possibilities for applications in confined spaces and liquid–air interfaces. The modeling process is presented in detail in Notes S2 and S3 in the supplementary information.

2.2 Water strider-inspired bipedal peristaltic locomotion mode

Water striders have evolved remarkable abilities to move efficiently on water surfaces using their specialized hydrophobic legs. Their exceptional water-walking ability stems from the hierarchical structure of their legs, which creates a superhydrophobic surface with contact angles exceeding 150°. This allows water striders to support forces up to 15 times their body weight on water surfaces, as illustrated in Fig. 2a. These natural principles have inspired the development of our novel BPLM for small-scale magnetic soft robots.

The BPLM is designed to enable efficient movement on liquid surfaces. In this mode, the front and tail of the robot maintain contact with the interface while the middle section is elevated (Fig. 2d). Under an alternating z-axis magnetic field, the robot performs controlled oscillations that facilitate rapid contact and separation from the liquid surface. The control waveform in the z-axis direction can be decomposed into two components: (1) a steady-state component that maintains the initial deformation in the *xoz* plane; (2) an oscillating component that induces small oscillations under deformation conditions (Fig. 2b). The deformation patterns of the upper and lower borders of the robot in the BPLM during locomotion are illustrated in Fig. 2c. The constant magnetic field in the x-axis direction shown in Fig. 2b leads to asymmetric deformation of the robot. This asymmetry causes the robot to move in a specific direction.

The movement speed of the robot is influenced by both the magnetic field strength and frequency. Experimental observations demonstrate that the velocity initially increases with the magnetic field frequency before reaching a peak at approximately 44 Hz. The magnetic field strength exhibits a similar effect with the movement speed increasing, reaching a threshold of up to 10 mT, beyond which the robot's gait stability is compromised.

2.3 *Pyrrhalta nymphaeae*-inspired single-region contact-vibration locomotion mode

Many small animals have evolved sophisticated strategies for navigating liquid–air interfaces. In particular, *Pyrrhalta nymphaeae* larvae exhibit remarkable meniscus climbing abilities (Fig. 2e). This natural phenomenon inspires the development of the SCLM, which enhances locomotion speed and stability through specialized back-arching mechanics. The SCLM implements a novel gait design in which the robot's

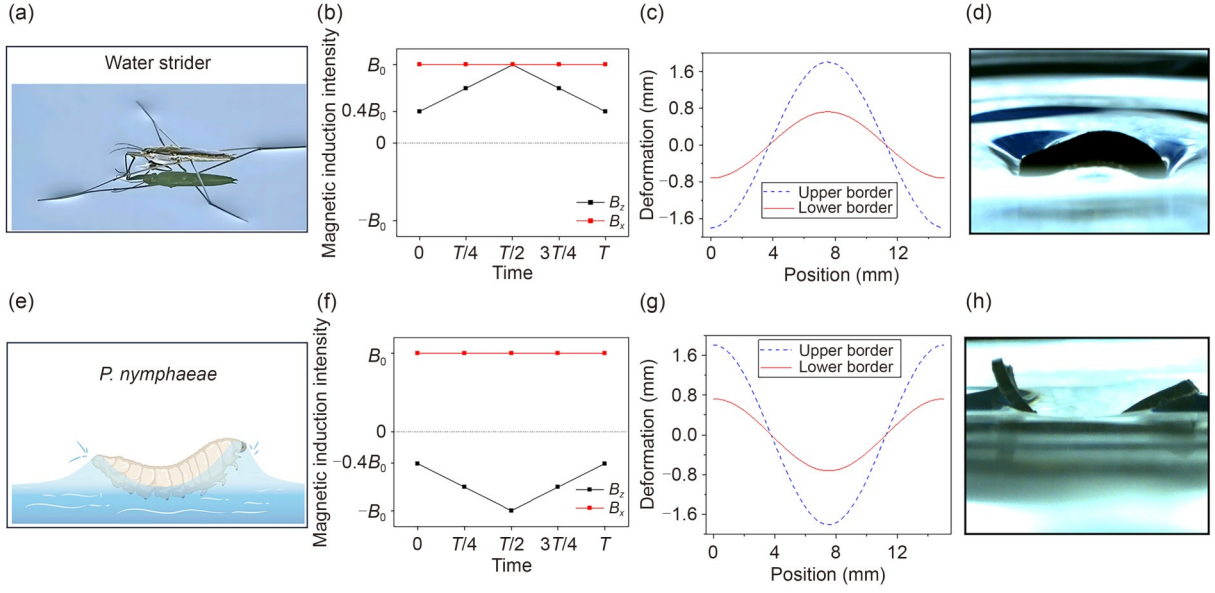

Fig. 2 Two types of bio-inspired locomotion modes: water strider-inspired BPLM and *Pyrrhalta nymphaeae*-inspired SCLM. (a, e) Biological inspirations for the two locomotion modes: a water strider walking on water and *Pyrrhalta nymphaeae* climbing on a liquid surface. (b, f) Temporal profiles of magnetic control signals with oscillation and steady-state components. (c, g) Deformation patterns of the robot's upper and lower borders during locomotion. (d, h) Experimental records showing the robot's interaction with the liquid surface for BPLM and SCLM. Videos S1 and S2 documenting the experiments are available in the supplementary information

back arches to contact the water surface, as illustrated in Fig. 2h. This configuration increases the contact area with the liquid surface, effectively preventing submersion while leveraging capillary forces for enhanced propulsion.

The control signal (Fig. 2f) comprises (1) an alternating magnetic field in the z-direction that generates initial deformation and slight vibrations; (2) a constant magnetic field component in the x-direction that determines movement direction. The deformation patterns of the upper and lower borders of the robot in the SCLM during locomotion are illustrated in Fig. 2g.

The robot's velocity v in this mode is given by [30]

$$v = \frac{2\pi^2}{L}(cYR)^2 f,$$

where Y represents the robot's maximum deformation amplitude during oscillation, f represents the traveling wave's frequency (coincident with the rotation frequency of B), c represents the correction coefficient accounting for external forces at the liquid surface, L represents the characteristic wavelength of motion, and R represents an approximated amplitude function of an ideal second-order system, which is defined as follows:

$$R = \begin{cases} 1, & f < \dfrac{\omega_{n,2}}{2\pi}, \\ \left(\dfrac{\omega_{n,2}}{2\pi f}\right)^2, & f \geqslant \dfrac{\omega_{n,2}}{2\pi}. \end{cases}$$

Here, $\omega_{n,2}$ is the second natural frequency of the robot.

3 Experimental setups

The experimental platform (Fig. 3a) is a sophisticated system designed to enable precise control and monitoring of the locomotion of the proposed magnetic soft robot. The platform incorporates several key components, including Helmholtz coils, a rotating base, an oscilloscope, and a vibration isolation platform.

The experimental environment (Fig. 3b) consists of a glass dish with a diameter of 110 mm and a height of 25 mm, partially filled with water to allow the robot to float. The controlled liquid environment is placed on the internal movement platform of the system. The platform design ensures that the robot can move freely without contact with the coils and that the liquid environment remains stationary even when the coils rotate.

The control process (Fig. 3c) begins with the generation of control signals using LabVIEW software on a personal computer (PC). These signals are transmitted via a PCIe-6738 card (National Instruments Corp., USA), which outputs an analog signal in the range of ±10 V. The signal is sent to the terminal box and then directed to the motor driver. The Helmholtz coils, which are essential for generating a controlled magnetic field, are powered by a high-power direct-current (DC) switch, ensuring the stability and precision of the magnetic environment. The parameters of the Helmholtz coils used in the experiments are listed in Table S1 (supplementary information). An industrial camera (MV-CA013-A0GM, Shenzhen City Celebr-Crystal Optoelectronic

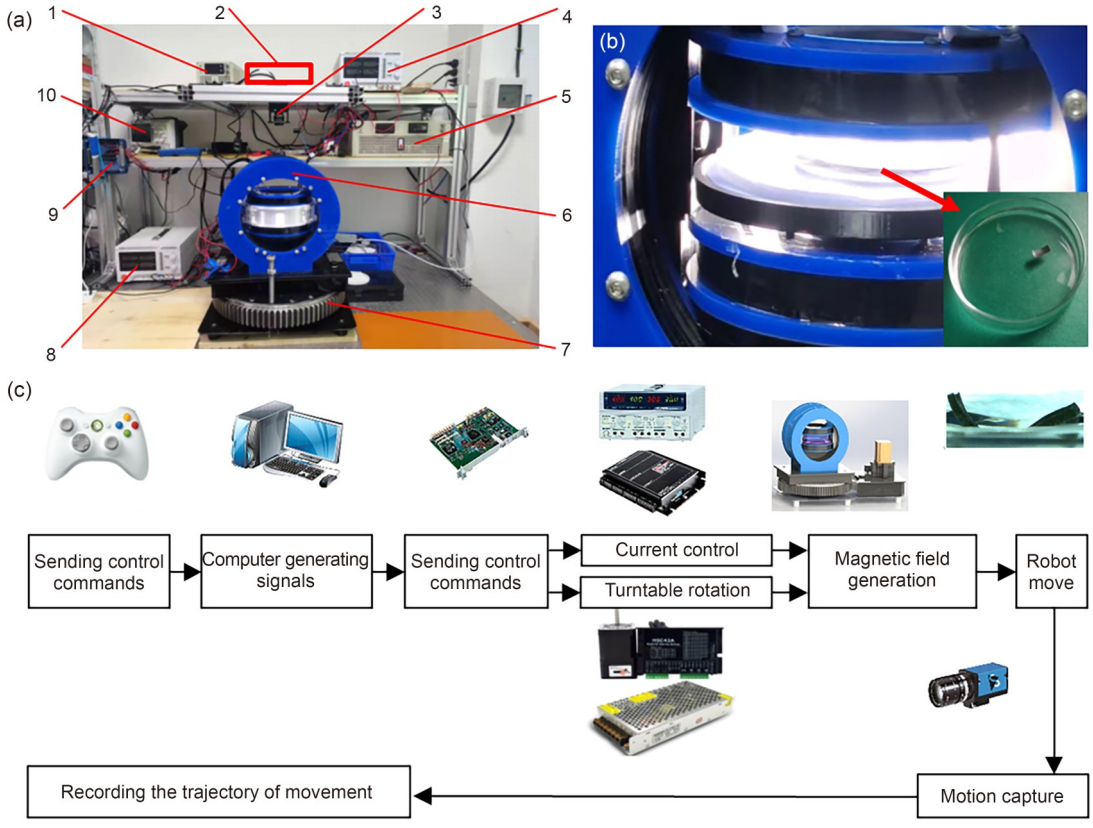

Fig. 3 Experimental setup and control roadmap for magnetic soft robot locomotion. (a) Magnetic drive platform utilizing a 3D Helmholtz coil system, detailing critical components (1. *z*-coil switch power supply; 2. *x*-coil and *z*-coil current driver; 3. *z*-axis camera; 4. 24-V DC voltage power supply at control end; 5. *x*-coil switch power supply; 6. two-dimensional Helmholtz coil; 7. a rotating base; 8. rotating base motor power supply; 9. card cable box; 10. oscilloscope). (b) Experimental workspace showing the proposed robot at the multiphase interface. (c) Control roadmap illustrating signal generation, field control, and motion capture processes

Ltd., China) captures the robot's motion within the plane, and the resulting motion images are processed using OpenCV on the PC. This enables real-time analysis of the robot's pose and movement trajectory, ensuring accurate monitoring and control.

4 Performance analysis

4.1 Robot deformation and locomotion

The motion and deformation characteristics of the magnetic soft robot were analyzed in the two locomotion modes. The robot's deformation under different magnetic field intensities was quantitatively analyzed by examining the front angle, rear angle, and deformation distance between the head and tail during the motion deformation process (Figs. 4a and 4e). In the experiments, magnetic fields of varying intensities were applied to the robot with the magnetic field control frequency set to 30 Hz. The robot's motion period was approximately 0.033 s, corresponding to one full cycle of motion.

Figures 4b–4d present the experimental results for the BPLM. The robot was subjected to alternating magnetic fields of 2.3, 5.5, 7.0, and 11.0 mT along the *z*-direction. Figure 4b illustrates the front angle variations over two consecutive cycles. During each cycle, the robot's front angle exhibits a trend of first increasing and then decreasing, which is consistent with the control waveform and the variation trend of the magnetic field intensity. This behavior is consistently observed under all magnetic field intensities. In addition, as the magnetic field intensity increases, the robot's front angle increases. Variations in the rear angle over two consecutive cycles are shown in Fig. 4c. Similar to the front angle, the rear angle exhibits a trend of first increasing and then decreasing during each cycle, and it exhibits a positive correlation with the magnetic field intensity. As the magnetic field intensity increases, the deformation distance exhibits more pronounced numerical changes, indicating that the robot's motion becomes more intense (Fig. 4d). For example, at lower field strengths, such as 2.3 mT, the robot exhibits minimal deformation, resulting in reduced propulsion efficiency. As the field intensity increases to 5.5 mT, the robot's deformation amplitude increases, varying from 14.5 to 12.2 mm, thereby enhancing forward propulsion. This deformation allows the robot to achieve wave-like motion

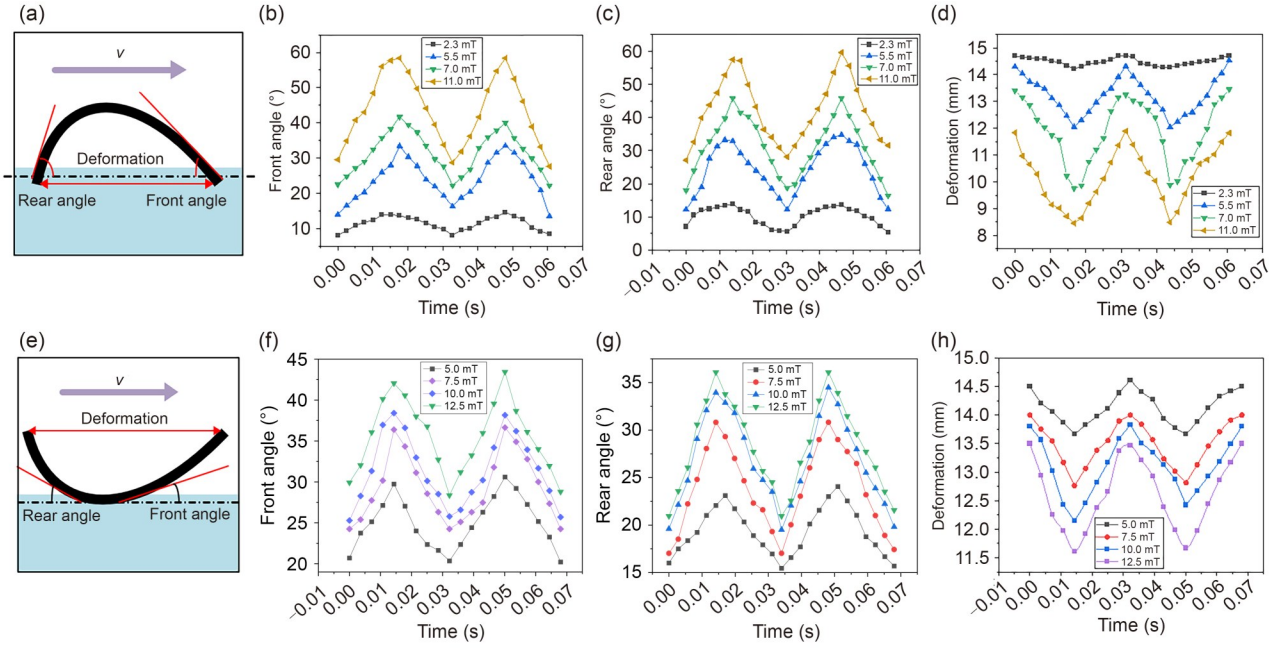

Fig. 4 Experimental results of motion and deformation under two locomotion modes. (a–d) Results for the BPLM showing the front angle, rear angle, and deformation distance between the head and tail during the robot's motion deformation process under magnetic field intensities of 2.3, 5.5, 7.0, and 11.0 mT. (e–h) Front angle, rear angle, and deformation distance between the head and tail during the robot's motion deformation process for the SCLM, where the single-region contact creates high deformation amplitudes under magnetic field intensities of 5.0, 7.5, 10.0, and 12.5 mT. The deformation dynamics differs between the two modes, with the BPLM promoting stability and the SCLM emphasizing higher propulsion speeds

along its length with synchronized oscillations between the front and rear angles. However, at 11.0 mT, the deformation becomes excessive, leading to potential instability, which causes inconsistencies in motion and reduces the overall propulsion efficiency.

Figures 4e–4h show the experimental results for the SCLM. This mode mimics the meniscus climbing behavior of *Pyrrhalta nymphaeae* larvae in which a single-region contact with a liquid surface drives the motion. The robot was subjected to alternating magnetic fields of 5.0, 7.5, 10.0, and 12.5 mT along the z-direction. Figures 4f and 4g show variations in the front and rear angles over two consecutive cycles, respectively. The variations in the robot's front and rear angles are generally consistent with the control waveform of the z-axis, showing a trend of first increasing and then decreasing, which is also consistent with the variation trend of the magnetic field intensity. A data comparison reveals that at any given moment, the robot's rear angle is consistently smaller than its front angle, which ensures the robot's forward movement direction. Figure 4h shows the variation trends of the deformation distance at the robot's head and tail over two consecutive cycles under magnetic field intensities of 5.0, 7.5, 10.0, and 12.5 mT. The deformation distance of the robot is inversely correlated with the control waveform along the z-axis, exhibiting a trend of first decreasing and then increasing. As the magnetic field intensity increases, the deformation distance exhibits more pronounced numerical changes, indicating that the robot's motion becomes more intense. For example, at lower field intensities (such as 5.0 mT), the robot exhibits moderate deformation with minimal oscillation amplitude and achieves stable but slow-forward motion. As the magnetic field intensity increases to 10.0 mT, the robot's deformation amplitude increases, varying from 13.7 to 12.2 mm, thereby enhancing forward propulsion. This increased deformation enhances propulsion efficiency, allowing the robot to achieve higher speeds than in the BPLM. At 12.5 mT, the deformation amplitude continues to increase; however, the oscillation pattern begins to lose symmetry, as shown in Fig. 4h. Asymmetry can cause lateral instabilities, which may affect the robot's trajectory and motion accuracy.

The two locomotion modes exhibit distinct motion and deformation dynamics. The BPLM achieves stable propulsion through periodic oscillations of two contact points with a liquid surface, thereby enabling a balance between deformation amplitude and stability. In contrast, the SCLM uses a single-region contact, which results in higher deformation amplitudes and greater propulsion speeds. For example, at optimal field strengths (7.5 mT for BPLM and 10.0 mT for SCLM), the SCLM achieves higher average speeds because of its larger deformation amplitude and enhanced utilization of capillary forces. However, the SCLM is more sensitive to excessive field intensities, where asymmetry in deformation patterns can lead to instability. In contrast, the BPLM demonstrates greater robustness under similar conditions,

making it more suitable for applications requiring consistent and stable trajectories.

4.2 Robot movement speed

The movement of the proposed robot is primarily caused by the continuous deformation and oscillation induced by the interaction between the robot and the driving magnetic field. The primary magnetic field parameters influencing this process are the magnetic field strength and frequency.

To demonstrate the changes in the robot's motion state under the driving frequency of the external magnetic field, Figs. 5a and 5c show the motion states of the robot in the BPLM and SCLM, respectively. These data were recorded using a camera at 0.1-s intervals over a 0.3-s motion cycle under an external magnetic field with a strength of 12 mT and driving frequencies of 4, 14, and 24 Hz. The results show that under the same magnetic field strength, the robot's locomotion speed exhibits a non-monotonic trend, increasing initially and then decreasing as the magnetic field frequency increases.

In addition, we analyzed the robot's motion variations under various magnetic field strengths, including 5.0, 7.5, 10.0, and 12.5 mT. Figures 5b and 5d present the experimental data analysis results corresponding to the BPLM and SCLM motion modes, respectively.

In the BPLM, the robot achieved a locomotion speed of approximately 20 mm/s under a magnetic field strength of 7.5 mT and an actuation frequency of 44 Hz, which corresponds to approximately 80 body lengths per minute (BL/min). Under continuous operation conditions, the robot covered a total locomotion distance of approximately 1100 mm within 1 min, with no noticeable degradation in posture or motion control capabilities.

By analyzing the curves in Fig. 5b, it can be observed that under the same magnetic field strength, the robot's motion speed first increases and then decreases as the frequency increases. This characteristic is evident across all magnetic field strengths, and the maximum speed is reached at approximately 44 Hz. When the magnetic field frequency exceeds 44 Hz, the robot's motion speed significantly decreases.

In addition, the magnetic field strength considerably influences the robot's motion speed. The results reveal that the robot's motion speed initially increases and then decreases as the magnetic field strength increases. When the magnetic field strength exceeds 7.5 mT, the robot's maximum motion speed gradually declines. The primary reasons for this include excessive deformation, which causes the front and rear angles of the robot to become too large, thereby reducing the horizontal component of the force acting on the robot. This decreases the propulsion force of the robot. Furthermore, as the vertical force component increases, the front

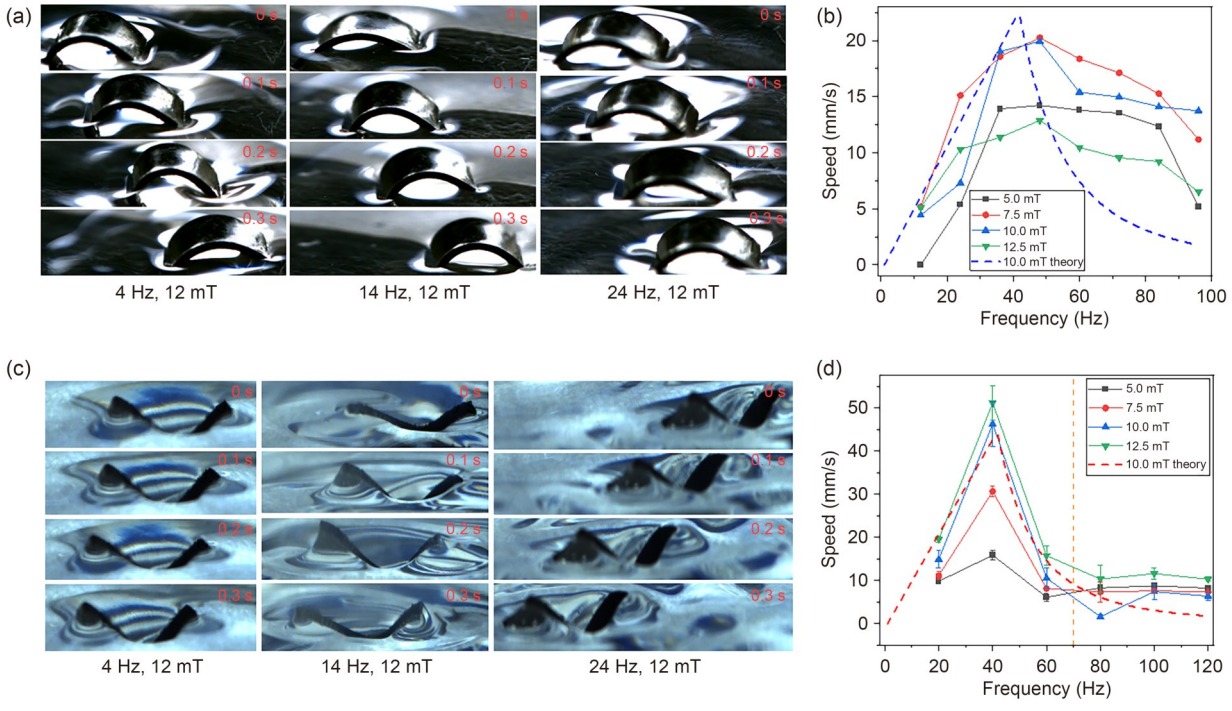

Fig. 5 Experimental results of robot movement speed under different locomotion modes and magnetic field parameters. BPLM results: (a) the robot's position over time under a 12-mT magnetic field at various frequencies; (b) the velocity curves at magnetic field strengths of 5.0, 7.5, 10.0, and 12.5 mT. SCLM results: (c) the robot's position over time under a 12-mT magnetic field at various frequencies; (d) the velocity curves at magnetic field strengths of 5.0, 7.5, 10.0, and 12.5 mT. Both modes exhibit a trend that speed increases with frequency up to an optimal point before declining

and rear ends of the robot become submerged below the water surface, increasing the resistance to forward motion.

In the SCLM, the robot's motion speed initially increases, then decreases, and eventually ceases as the magnetic field frequency changes. At a magnetic field frequency of 40 Hz, the robot's average locomotion speed reaches approximately 52 mm/s (equivalent to 208 BL/min). The robot exhibited stable locomotion performance over a sustainable operation period of 1 min and covered a total locomotion distance of approximately 2950 mm without any noticeable degradation in its posture or motion control abilities. When the magnetic field frequency exceeds 70 Hz, the robot's motion speed remains relatively low without significant variations. In addition, when the frequency is less than 70 Hz, under a constant magnetic field strength, the robot's motion speed initially increases and then decreases as the magnetic field frequency increases, eventually stabilizing at a relatively low level. At the same magnetic field control frequency, the robot's motion speed increases with increasing magnetic field strength. However, when the magnetic field control frequency exceeds 70 Hz, neither increasing the magnetic field strength nor the magnetic field frequency significantly increases the robot's motion speed.

Using a beam structure model from the mechanics of materials, we calculated the robot's first-order natural frequency as 40.73 Hz. When the robot achieves its maximum motion speed, the driving frequency is 44 Hz for the BPLM and 40 Hz for the SCLM, both of which exhibit certain deviations from the theoretical results. These deviations are primarily attributed to the fact that the two ends of the robot are not completely free, thereby introducing theoretical errors. The theoretical relationship between the robot's motion speed and the driving magnetic field frequency for the BPLM and SCLM under a 10.0-mT magnetic field strength is represented by the blue and red dashed lines in Figs. 5b and 5d, respectively. Our experimental measurements are consistent with the theoretical model.

4.3 Analysis of robot motion trajectory

The motion trajectory of the proposed magnetic soft robot is a critical aspect of its performance, particularly for precision tasks such as object manipulation and navigation in confined spaces. The experimental results demonstrate the ability of the robot to execute straight-line, reciprocal, rotational, and circular motions under both locomotion modes.

Linear motion and directional control: In the BPLM, the robot's head and tail alternate their contact with the liquid surface, enabling precise linear motion. As shown in Fig. 6a, the robot moves left and right within the same interval under

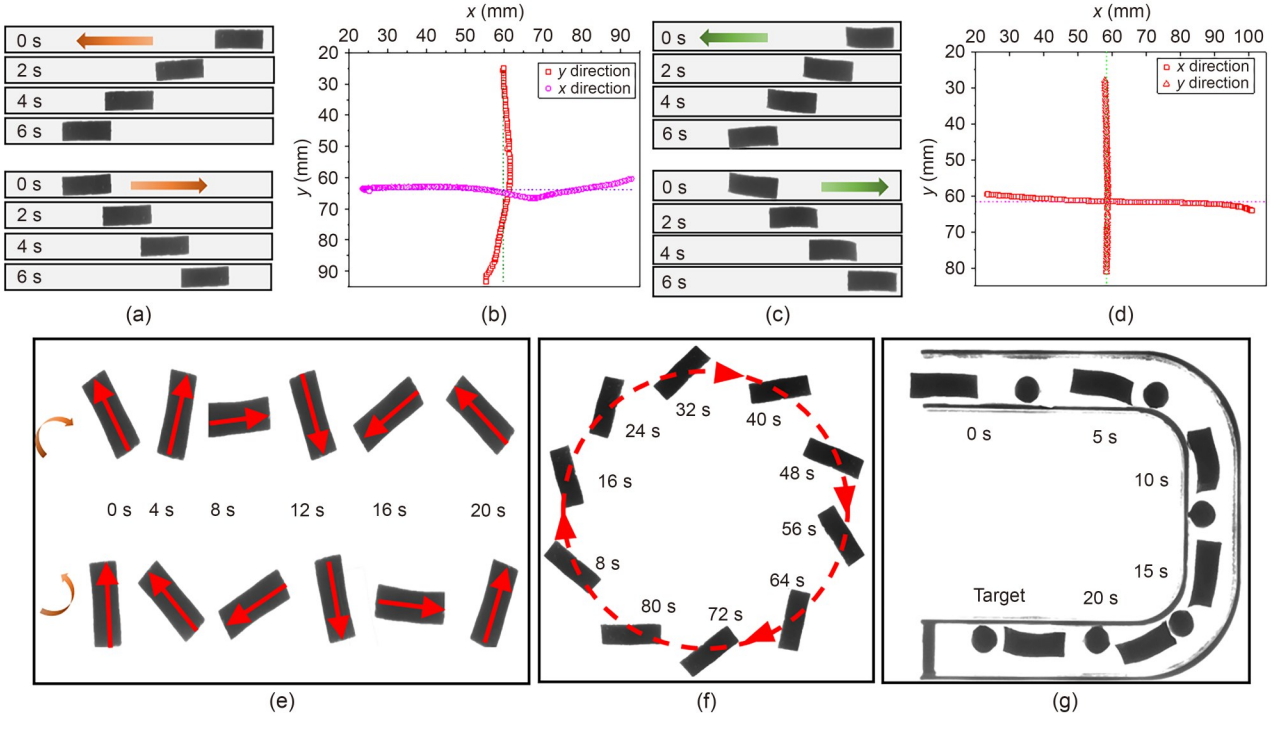

Fig. 6 Characterization of robot motion performance under different modes. (a) The robot performs linear reciprocal motion in BPLM. (b) Tracking data for BPLM show minimal errors in the *x*- and *y*-direction (1.288 and 1.549 mm, respectively). (c) The robot performs linear reciprocal motion in SCLM. (d) Tracking data for SCLM demonstrate improved precision with positional errors of 1.028 mm in the *x*-direction and 0.207 mm in the *y*-direction. (e) The robot exhibits clockwise and counterclockwise rotational motions. (f) The robot follows a circular trajectory guided by a magnetic field. (g) The robot transports a spherical object through an anti-"C"-shaped confined space and reaches the target position within 20 s. BPLM was used in (e, f, g)

open-loop control, achieving consistent trajectories with minimal lateral deviation. The corresponding tracking data shown in Fig. 6b demonstrate the linear motion accuracy characterized by the standard deviation in this mode. The measured positional errors are 1.288 and 1.549 mm in the *x*- and *y*-direction, respectively, demonstrating the ability of the robot to maintain a straight path over time.

In the SCLM, the robot relies on single-region contact with the liquid surface. Figure 6c illustrates the robot's reciprocal motion to the left and right in this mode. Figure 6d tracks the linear trajectory of the robot. This mode exhibits even smaller positional errors of 1.028 and 0.207 mm in the *x*- and *y*-direction, respectively, indicating improved motion precision compared to the BPLM.

Rotational and circular motions: The proposed robot also exhibits excellent rotational maneuverability. As shown in Fig. 6e, the robot performs clockwise and counterclockwise rotations on the water surface. The robot's steering is achieved through the rotation of the magnetic field around the *z*-axis, and the turntable at the bottom of the magnetic control platform enables this process. In addition, the robot moves along circular trajectories (Fig. 6f). This is accomplished by continuously altering the magnetic field orientation in a controlled manner, resulting in smooth circular motion. Such capabilities are crucial for tasks requiring agile navigation, such as avoiding obstacles or following curved paths.

Navigation in confined spaces: One of the most remarkable achievements of the proposed robot is its ability to navigate confined spaces. Figure 6g illustrates the robot pushing a spherical object through an anti-"C"-shaped confined space at a liquid–air interface. Guided by the magnetic field, the robot successfully transported the object to a specific target position within 20 s, demonstrating its potential for precise and efficient object manipulation in constrained environments.

The BPLM excels at maintaining stable linear trajectories, whereas the SCLM offers improved precision with smaller positional errors. The proposed robot's ability to perform rotational and circular motions, combined with its effectiveness in navigating confined spaces, highlights its potential for various applications, including precision object manipulation and agile navigation.

5 Conclusions and discussion

Drawing inspiration from water striders and *Pyrrhalta nymphaeae* larvae, we designed and developed a magnetic robot that achieves efficient and versatile locomotion at liquid–air interfaces. The BPLM and SCLM can be used in various applications, including precision navigation, object manipulation, and operations in confined spaces.

The BPLM leverages alternating contact points to produce stable and efficient propulsion. This mode exhibits excellent linear motion performance with minimal trajectory errors (1.288 mm in the *x*-direction and 1.549 mm in the *y*-direction). It also achieves optimal locomotion speeds at moderate magnetic field strengths (7.5 mT) and frequencies (44 Hz). However, excessive magnetic field intensity can disrupt gait stability and reduce propulsion efficiency. The SCLM demonstrates superior speed and precision because of its single-region contact mechanism. With smaller trajectory errors (1.028 mm in the *x*-direction and 0.207 mm in the *y*-direction), this mode achieves higher velocity peaks, particularly at field strengths of approximately 10.0 mT. However, its sensitivity to high field intensities and frequencies poses challenges related to motion stability. Both modes excel in terms of agility and maneuverability, enabling the proposed robot to perform rotational, circular, and confined space motions. The proposed robot successfully executes object manipulation tasks, thereby highlighting its capability for precise and efficient operations in constrained environments. Although both locomotion modes achieve efficient propulsion, the trade-off between stability and speed must be carefully considered for specific applications. The BPLM is well-suited for tasks requiring robust and consistent trajectories, whereas the SCLM is ideal for applications requiring high speed and precision.

The experimental results validate the theoretical models for robot deformation and motion dynamics. The close agreement between the experimental and theoretical velocity curves, particularly in the SCLM, indicates the accuracy of the mathematical framework. However, discrepancies at higher field intensities suggest that further refinements are required to account for nonlinear effects such as hydrodynamic resistance and instability.

Future research can focus on closed-loop control systems and enhanced application-specific robot optimization design to further improve the performance and versatility of the proposed robot.

Supplementary Information The online version contains supplementary material available at https://doi.org/10.1631/bdm.2500047.

Acknowledgements This work was supported by the Shenzhen Science and Technology Program (Nos. JCYJ20210324132810026, KQTD20210811090146075, and GXWD20220811164014001), the National Natural Science Foundation of China (Nos. 52375175, 52005128, 62473277, and 52475075), the National Key Research and Development Program of China (No. 2022YFC3802302), Guangdong Basic and Applied Basic Research Foundation (No. 2024A1515240015), Jiangsu Provincial Outstanding Youth Program (No. BK20230072), Suzhou Industrial Foresight and Key Core Technology Project (No. SYC2022044), a grant from Open Foundation of the State Key Laboratory of Fluid Power and Mechatronic Systems, and grants from Jiangsu Qinglan Project and Jiangsu 333 High-level Talents.

Author contributions CLH and BHD were involved in conceptualization and writing the original draft. HCW, SHY, LZ, and BL assisted in the investigation and writing. FZN and DH conducted a deep review and editing. HYY offered advice. QC, FZN, and DH helped revise the paper, supervised the work, and applied for funds. CLH and SHY made the revisions. All authors have read and approved the manuscript for publication.

Declarations

Conflict of interest HYY is an editor-in-chief, DH is an academic editor, and FZN is a young academic editor for *Bio-Design and Manufacturing*; they were not involved in the editorial review or the decision to publish this article. The authors declare that they have no conflict of interest.

Ethical approval This study does not contain any studies with human or animal subjects performed by any of the authors.

Data availability The data that support the findings of this study are available from the corresponding authors upon reasonable request.

References

1. Lee H, Kim DI, Kwon SH et al (2021) Magnetically actuated drug delivery helical microrobot with magnetic nanoparticle retrieval ability. ACS Appl Mater Interfaces 13(17):19633–19647. https://doi.org/10.1021/acsami.1c01742
2. Ebrahimi N, Bi CH, Cappelleri DJ et al (2021) Magnetic actuation methods in bio/soft robotics. Adv Funct Materials 31(11):2005137. https://doi.org/10.1002/adfm.202005137
3. Dong Y, Wang L, Xia N et al (2022) Untethered small-scale magnetic soft robot with programmable magnetization and integrated multifunctional modules. Sci Adv 8(25):eabn8932. https://doi.org/10.1126/sciadv.abn8932
4. Nelson BJ, Gervasoni S, Chiu PWY et al (2022) Magnetically actuated medical robots: an in vivo perspective. Proc IEEE 110(7): 1028–1037. https://doi.org/10.1109/JPROC.2022.3165713
5. Kim Y, Zhao XH (2022) Magnetic soft materials and robots. Chem Rev 122(5):5317–5364. https://doi.org/10.1021/acs.chemrev.1c00481
6. Chen MH, Liu ZW, Li YK et al (2024) Magnetic nanofluid-based liquid marble for a self-powered mechanosensation. Droplet 3(3):e122. https://doi.org/10.1002/dro2.122
7. Chung HJ, Parsons AM, Zheng LL (2021) Magnetically controlled soft robotics utilizing elastomers and gels in actuation: a review. Adv Intell Syst 3(3):2000186. https://doi.org/10.1002/aisy.202000186
8. Eshaghi M, Ghasemi M, Khorshidi K (2021) Design, manufacturing and applications of small-scale magnetic soft robots. Extreme Mech Lett 44:101268. https://doi.org/10.1016/j.eml.2021.101268
9. Tang W, Gao YD, Dong ZY et al (2024) Sustainable and untethered soft robots created using printable and recyclable ferromagnetic fibers. Bio-Des Manuf 7(6):926–937. https://doi.org/10.1007/s42242-024-00303-4
10. Wang TL, Wu YD, Yildiz E et al (2024) Clinical translation of wireless soft robotic medical devices. Nat Rev Bioeng 2(6):470–485. https://doi.org/10.1038/s44222-024-00156-7
11. Huo YX, Yang LD, Xu TT et al (2025) Design, control, and clinical applications of magnetic actuation systems: challenges and opportunities. Adv Intell Syst 7(3):2400403. https://doi.org/10.1002/aisy.202400403
12. Du XZ, Yu JF (2023) Image-integrated magnetic actuation systems for localization and remote actuation of medical miniature robots: a survey. IEEE Trans Robot 39(4):2549–2568. https://doi.org/10.1109/TRO.2023.3271582
13. Lin ZN, Jiang T, Shang JZ (2022) The emerging technology of biohybrid micro-robots: a review. Bio-Des Manuf 5(1):107–132. https://doi.org/10.1007/s42242-021-00135-6
14. Huang HW, Sakar MS, Petruska AJ et al (2016) Soft micromachines with programmable motility and morphology. Nat Commun 7:12263. https://doi.org/10.1038/ncomms12263
15. Hu CZ, Pané S, Nelson BJ (2018) Soft micro- and nanorobotics. Annu Rev Control Robot Auton Syst 1:53–75. https://doi.org/10.1146/annurev-control-060117-104947
16. Cao Q, Pan Y, Zhang YQH et al (2025) A dual-functional capsule robot for drug delivery and tissue biopsy based on magnetic torsion spring technology. Bio-Des Manuf 8(3):495–510. https://doi.org/10.1631/bdm.2400276
17. Ren ZY, Zhang RJ, Soon RH et al (2021) Soft-bodied adaptive multimodal locomotion strategies in fluid-filled confined spaces. Sci Adv 7(27):eabh2022. https://doi.org/10.1126/sciadv.abh2022
18. Gu HR, Boehler Q, Cui HY et al (2020) Magnetic cilia carpets with programmable metachronal waves. Nat Commun 11(1):2637. https://doi.org/10.1038/s41467-020-16458-4
19. Wang QQ, Tian Y, Du XZ et al (2022) Magnetic navigation of collective cell microrobots in blood under ultrasound Doppler imaging. IEEE/ASME Trans Mechatron 27(5):3174–3185. https://doi.org/10.1109/TMECH.2021.3109346
20. Lu HJ, Zhang M, Yang YY et al (2018) A bioinspired multilegged soft millirobot that functions in both dry and wet conditions. Nat Commun 9(1):3944. https://doi.org/10.1038/s41467-018-06491-9
21. Niu F, Xue Q, Cao Q et al (2025) Magneto-soft robots based on multi-materials optimizing and heat-assisted in-situ magnetic domains programming. Int J Extrem Manuf 7(5):055506. https://doi.org/10.1088/2631-7990/add81b
22. Han ZW, Mu ZZ, Yin W et al (2016) Biomimetic multifunctional surfaces inspired from animals. Adv Colloid Interface Sci 234: 27–50. https://doi.org/10.1016/j.cis.2016.03.004
23. Li TL, Yu SM, Sun B et al (2023) Bioinspired claw-engaged and biolubricated swimming microrobots creating active retention in blood vessels. Sci Adv 9(18):eadg4501. https://doi.org/10.1126/sciadv.adg4501
24. Zhang C, Zhu PG, Lin YQ et al (2021) Fluid-driven artificial muscles: bio-design, manufacturing, sensing, control, and applications. Bio-Des Manuf 4(1):123–145. https://doi.org/10.1007/s42242-020-00099-z
25. Bai XH, Peng YH, Li DZ et al (2024) Novel soft robotic finger model driven by electrohydrodynamic (EHD) pump. J Zhejiang Univ Sci A 25(7):596–604. https://doi.org/10.1631/jzus.A2300479
26. Song YS, Sitti M (2007) Surface-tension-driven biologically inspired water strider robots: theory and experiments. IEEE Trans Robot 23(3):578–589. https://doi.org/10.1109/TRO.2007.895075
27. Liu JH, Shen MJ, Ma ZQ et al (2024) Research progress on bionic water strider robots. J Bionic Eng 21(2):635–652. https://doi.org/10.1007/s42235-023-00467-2
28. Huang CQ, Pinchin NP, Lin CH et al (2024) Self-propelled morphing matter for small-scale swimming soft robots. Adv Funct Mater 34(52):2413129. https://doi.org/10.1002/adfm.202413129
29. Liao MJ, Shen CY, Liu CH et al (2024) Larva-inspired drilling robot. In: International Conference on Advanced Robotics and Intelligent Systems, p.1–6. https://doi.org/10.1109/ARIS62416.2024.10679968
30. Hu WQ, Lum GZ, Mastrangeli M et al (2018) Small-scale soft-bodied robot with multimodal locomotion. Nature 554(7690): 81–85. https://doi.org/10.1038/nature25443